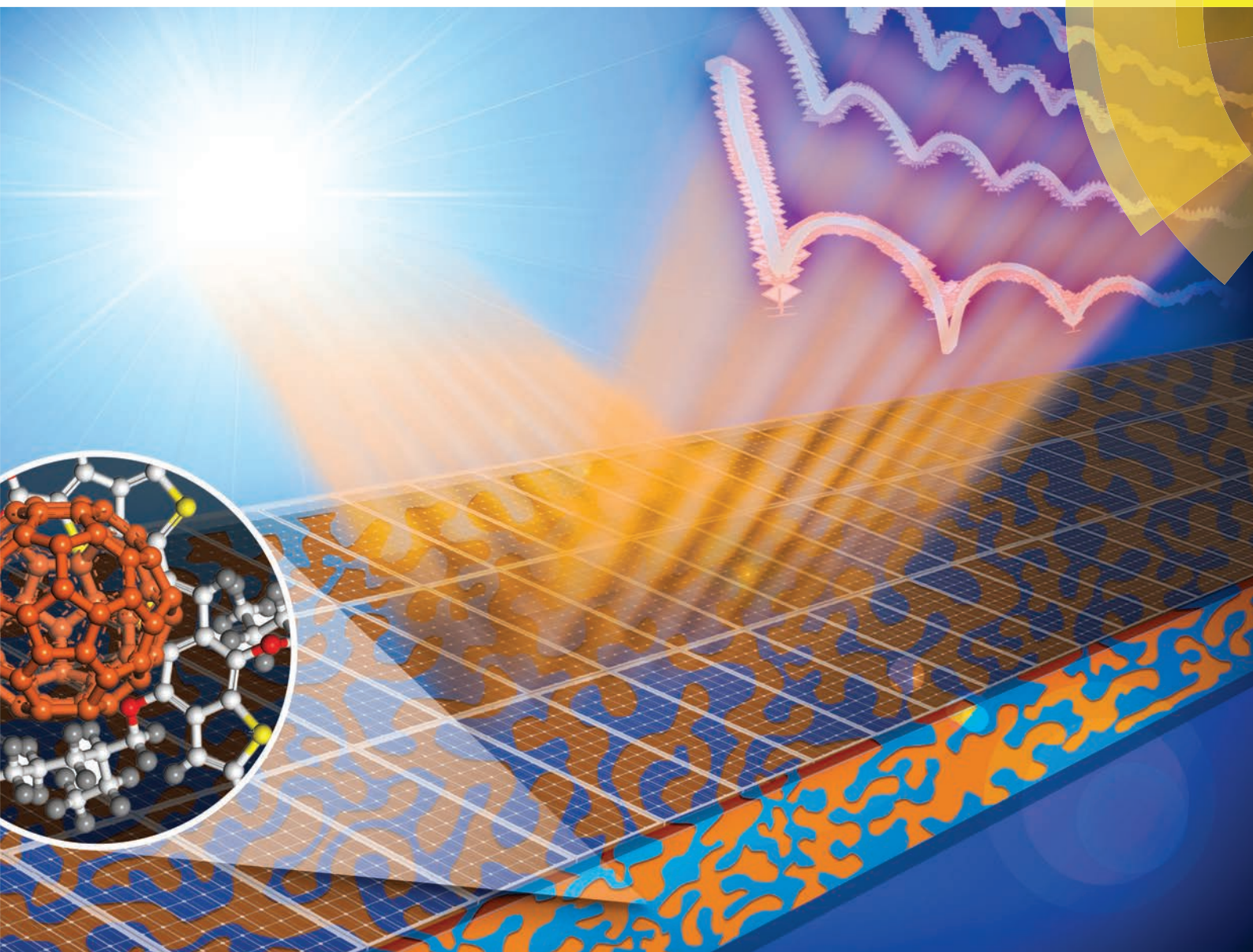


Nanoscale

www.rsc.org/nanoscale



ISSN 2040-3364



COMMUNICATION

Jong K. Keum, Kai Xiao *et al.*

Correlating high power conversion efficiency of PTB7:PC₇₁BM inverted organic solar cells with nanoscale structures





Cite this: *Nanoscale*, 2015, 7, 15576

Received 20th May 2015,
 Accepted 10th July 2015
 DOI: 10.1039/c5nr03332b
www.rsc.org/nanoscale

Correlating high power conversion efficiency of PTB7:PC₇₁BM inverted organic solar cells with nanoscale structures†

Sanjib Das,^a Jong K. Keum,^{*b,c} James F. Browning,^c Gong Gu,^a Bin Yang,^b Ondrej Dyck,^d Changwoo Do,^c Wei Chen,^{e,f} Jihua Chen,^b Ilia N. Ivanov,^b Kunlun Hong,^b Adam J. Rondinone,^b Pooran C. Joshi,^g David B. Geohegan,^b Gerd Duscher^d and Kai Xiao^{*b}

Advances in material design and device engineering led to inverted organic solar cells (i-OSCs) with superior power conversion efficiencies (PCEs) compared to their “conventional” counterparts, in addition to the well-known better ambient stability. Here, we report an in-depth morphology study of the i-OSC active and cathode modifying layers, employing a model system with a well-established bulk-heterojunction, PTB7:PC₇₁BM as the active layer and poly-[(9,9-bis(3′-(*N,N*-dimethylamino)propyl)-2,7-fluorene)-*alt*-2,7-(9,9-dioctylfluorene)] (PFN) as the cathode surface modifying layer. We have also identified the role of a processing additive, 1,8-diiodooctane (DIO), used in the spin-casting of the active layer to increase PCE. Using various characterization techniques, we demonstrate that the high PCEs of i-OSCs are due to the diffusion of electron-accepting PC₇₁BM into the PFN layer, resulting in improved electron transport. The diffusion occurs when residual solvent molecules in the spun-cast film act as a plasticizer. Addition of DIO to the casting solution results in more PC₇₁BM diffusion and therefore more efficient electron transport. This work provides important insight and guidance to further enhancement of i-OSC performance by materials and interface engineering.

Organic solar cells (OSCs) have attracted tremendous attention as next-generation photovoltaics due to their potential for generating electricity at a low cost and compatibility with flexible

substrates required for roll-to-roll manufacturing.^{1–4} In the past decade, various efforts such as thermal annealing,^{5,6} solvent-vapor annealing,^{7,8} use of processing additives^{9–11} and solvent mixture,^{12,13} material design,¹⁴ and interface and band gap engineering^{15–17} have been expended to improve the power conversion efficiencies (PCEs) of OSCs.¹⁸

Compared with the conventional organic solar cells (c-OSCs), where the hygroscopic and corrosive poly(3,4-ethylene-dioxythiophene):poly(styrenesulfonate acid) (PEDOT:PSS) hole transport layer and a low work function metal top electrode are detrimental to device lifetime, inverted organic solar cells (i-OSCs) exhibit significantly improved stability under ambient conditions by avoiding these major contributors to device degradation.^{19–22} Despite the outstanding long-term device stability, however, early i-OSCs suffered from lower PCE as compared with c-OSCs.^{23,24} Moreover, most early i-OSCs used n-type metal oxides such as TiO_x as the hole blocking layer, requiring high-temperature sintering,^{24,25} undesirable for flexible substrates preferred for roll-to-roll manufacturing. Most recently, a thin layer of conjugated polymer, poly [(9,9-bis(3′-(*N,N*-dimethylamino)propyl)-2,7-fluorene)-*alt*-2,7-(9,9-dioctylfluorene)] (PFN) (see Scheme S1, ESI†), was used as a surface modifier for the indium tin oxide (ITO) bottom electrode to drastically reduce the energetic misalignment between ITO and the active layer, resulting in ohmic contact between the two.²⁶ Beside achieving a record PCE of 9.2% and ambient device stability exceeding 60 days, the room-temperature, solution-processed PFN is favorable for flexible and large-scale roll-to-roll production.⁴ These high-performance i-OSCs employed poly[[4,8-bis[(2-ethylhexyl)oxy]benzo[1,2-*b*:4,5-*b'*]dithiophene-2,6-diyl][3-fluoro-2-[(2-ethylhexyl)carbonyl]thieno[3,4-*b*]thiophenediyl]] (PTB7) as the electron donor (ED) and [6,6]-phenyl C₇₁-butyric acid methyl ester (PC₇₁BM) as the electron acceptor (EA). Further progress by synthesizing a new polymer semiconductor to replace PTB7 has demonstrated a record PCE exceeding 10% for this device architecture.²⁷

Despite the above-mentioned progress, the morphological mechanism for the high PCE of these devices remains to be

^aDepartment of Electrical Engineering and Computer Science, University of Tennessee, Knoxville, TN 37996, USA

^bCenter for Nanophase Materials Sciences, Oak Ridge National Laboratory, Oak Ridge, TN 37831, USA. E-mail: keumjk@ornl.gov, xiaok@ornl.gov

^cNeutron Sciences Directorate, Oak Ridge National Laboratory, Oak Ridge, TN 37831, USA

^dDepartment of Materials Science and Engineering, University of Tennessee, Knoxville, TN 37996, USA

^eMaterials Science Division, Argonne National Laboratory, Lemont, IL 60439, USA

^fInstitute for Molecular Engineering, The University of Chicago, Chicago, IL 60637, USA

^gMaterials Science and Technology Division, Oak Ridge National Laboratory, Oak Ridge, TN 37831, USA

† Electronic supplementary information (ESI) available. See DOI: 10.1039/c5nr03332b

investigated. Specifically, it has so far been unclear how the morphologies of the active layer and the active layer/PFN interface impact i-OSC operation and the associated efficiency. In this work, we focused our efforts on understanding how PFN interacts with PTB7 and PC₇₁BM at the interface, affects the active layer morphologies, and enhances the PCEs of the i-OSCs. The lateral and vertical phase morphologies of PFN/PTB7:PC₇₁BM were studied by a combination of neutron reflectometry (NR) and cross-section transmission electron microscopy (TEM). Grazing incidence wide-angle X-ray scattering (GIWAXS) was used to study the relative crystallinity and crystal orientation. In addition, small-angle neutron scattering (SANS) was used to study the precursor structures of PTB7 and PC₇₁BM in the casting solution, as well as the effect of the solvent additive 1,8-diiodooctane (DIO). The obtained structural information was linked to measured device performance, provide important guidance to the design of more efficient i-OSCs.

Fig. 1a shows the current density *versus* voltage (J - V) characteristics for a typical solar cell of each of the following architecture-processing combinations: ITO/PFN (10 nm)/active layer/MoO₃(8 nm)/Ag i-OSCs with and without a 3 wt% DIO additive in the PTB7:PC₇₁BM-in-1,2-dichlorobenzene (DCB) solution for spin-casting the active layer; and ITO/PEDOT:PSS (40 nm)/active layer/Ca (15 nm)/Al c-OSCs with and without a 3 wt%

DIO additive when spin-casting the PTB7:PC₇₁BM active layer. Detailed device fabrication is described in the ESI.† The device performance parameters, *i.e.*, short-circuit current density (J_{SC}), open circuit voltage (V_{OC}), fill factor (FF), and PCE, listed in Table 1 clearly show that i-OSCs with and without DIO exhibit higher PCEs than their c-OSC counterparts and that the DIO additive increases PCEs for both i-OSCs and c-OSCs. The superior performance of the i-OSCs is attributed to efficient charge extraction by the ITO cathode the effective work function of which is drastically modified by PFN.^{26,27} Here, PTB7:PC₇₁BM i-OSCs fabricated with 3 wt% DIO exhibit PCE as high as 9.3%, much higher than the c-OSCs fabricated using the same solution showing a maximum PCE of 7.2% (Fig. S1†). Also, the i-OSCs retain ~94% of their initial PCEs up to more than 26 days when stored in air while OSCs lose 30% of their initial PCE in just 5 days (Fig. S2†). The higher PCEs of i-OSCs, compared to those of c-OSCs, are due to their higher J_{SC} values, confirming that this is the result of efficient electron extraction. The external quantum efficiency (EQE) spectra of the same devices in Fig. 1a, recorded under short circuit conditions in air without encapsulations, are shown in Fig. 1b. The integrated J_{SC} values of i-OSCs, with and without DIO from EQE spectra, are 16.6 and 15.9 mA cm⁻², respectively, while those of c-OSCs are 14.1

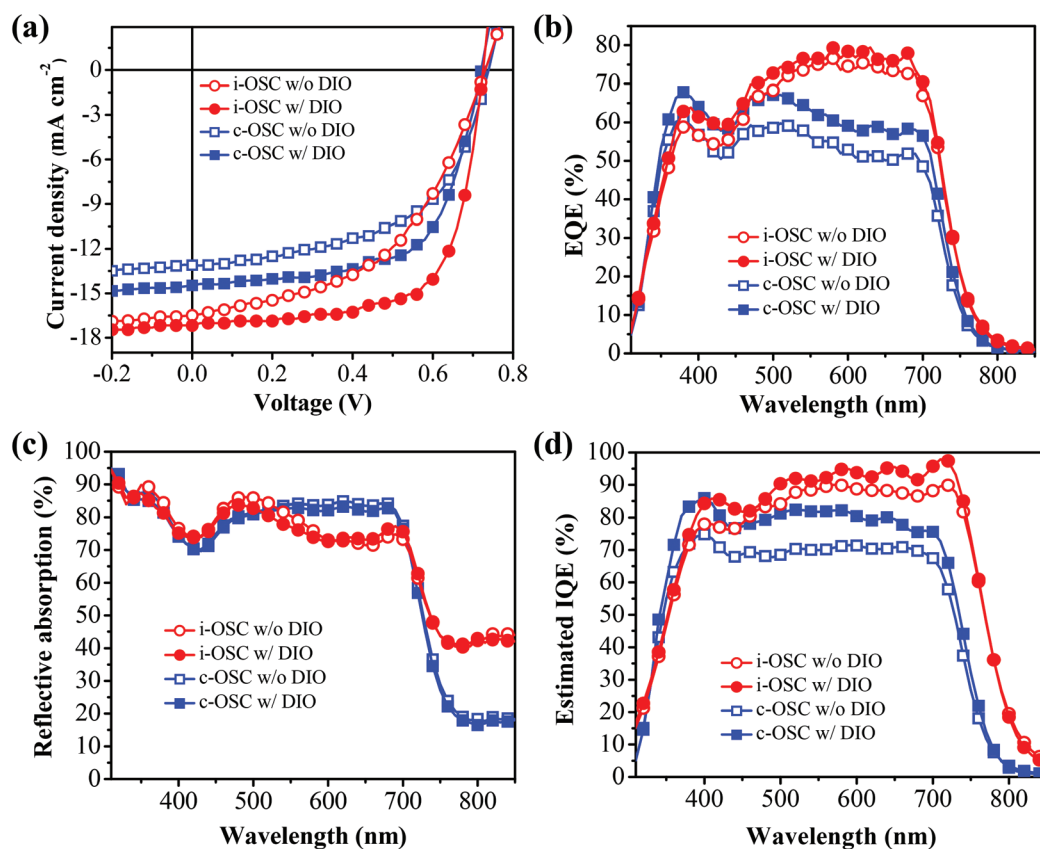


Fig. 1 (a) J - V curves for devices with different architecture-processing combinations. (b) EQE spectra for the corresponding devices. (c) Reflective absorption spectra *versus* wavelength. (d) Estimated IQE calculated using the results from (b) and (c).

Table 1 Summary of device performance parameters, *i.e.*, J_{SC} , V_{OC} , FF, and PCE of the OPV devices based on PTB7:PC₇₁BM (1:1.5) with or without DIO

Device type	J_{SC} (mA cm ⁻²)	V_{OC} (V)	FF (%)	PCE _{avg} ^a (%)	PCE _{max} (%)
i-OSC w/o DIO	15.3	0.72	47.8	5.3 ± 0.3	5.8
i-OSC w/ DIO	16.9	0.72	67.0	8.2 ± 0.5	9.3
c-OSC w/o DIO	12.9	0.74	52.7	5.0 ± 0.3	5.5
c-OSC w/ DIO	14.4	0.72	62.3	6.5 ± 0.3	7.2

^a Average PCE for each type was calculated from over 20 devices, measured under AM 1.5 G (100 mW cm⁻²) illumination.

and 12.4 mA cm⁻², reasonably well-consistent with the J_{SC} values, measured from J - V curves in an inert ambient. To estimate the internal quantum efficiency (IQE) spectra, the reflective absorption spectrum for each architecture-processing combination (Fig. 1c) was first measured mimicking the light absorption process in an actual device. Here it should be noted that IQE is defined as the percentage of absorbed photons that are converted into charges and collected at the electrodes at zero bias. The IQE spectra were recorded by following the procedures reported elsewhere.^{28,29} Irrespective of the presence of DIO, i-OSCs show higher IQE compared to c-OSCs. The DIO additive increases the IQEs for both the i-OSCs and c-OSCs, and more importantly, the i-OSC using DIO shows an IQE approaching 95% in the 500–700 nm spectral range. In principle, the high IQE originates from highly efficient exciton generation and dissociation, and charge collection.

To understand the origin of the near-unity IQE, we employed a variety of characterization techniques to systematically examine the PTB7:PC₇₁BM active film morphology in the i-OSCs as well as processing factors that influence the morphology. It has been shown that the initial precursor structures of electron donor (ED) and acceptor (EA) materials in the casting solution affect the crystallinity and phase morphology of the spun-cast films.³⁰ Here, we conducted small-angle neutron scattering (SANS) measurements on the PTB7 and PC₇₁BM solutions in DCB with and without DIO to investigate the structure of PTB7 (ED) and PC₇₁BM (EA) in the solutions, and the effect of DIO. As seen from the SANS curves in Fig. 2, both PC₇₁BM solutions in DCB and DCB:DIO merely exhibit flat scattering features, implying complete dissolution. If PC₇₁BM forms aggregates or clusters in the solutions, scattering features, showing an asymptotic decay in scattered intensity as a function of the scattering vector q , must be observed. Here, the scattering vector is defined as $q = 4\pi \sin \theta / \lambda$, where λ and θ are the wavelength of the incident neutron beam and the half of scattering angle, respectively. The results are consistent with the previous work reported elsewhere by current authors showing complete dissolution of PC₇₁BM in DCB and DCB:DIO.³¹ We have noticed possibly contradicting results reported by Lou *et al.* based on the small-angle X-ray scattering (SAXS),³² indicating that the added DIO selectively increases

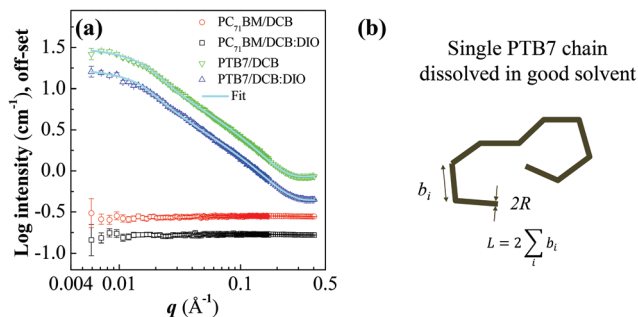


Fig. 2 (a) SANS patterns for PTB7/DCB, PTB7/DCB:DIO, PC₇₁BM/DCB, and PC₇₁BM/DCB:DIO solutions, where the solid lines indicate model fits by a flexible cylinder scattering model with an excluded volume effect. (b) Schematic illustration of a single PTB7 chain dissolved in DCB or DCB:DIO.

the solubility of PC₇₁BM when mixed with the host solvent, chlorobenzene (CB). In the study, it was proposed that the added DIO selectively increases the solubility of PC₇₁BM when mixed with CB, resulting in a reduced domain size of PC₇₁BM in the spun-cast active layer. In our current and previous studies, however, used solvents, DCB and DCB:DIO are found to dissolve PC₇₁BM at the molecular level. The different conclusions might come from the solubility difference between CB and DCB. On the other hand, the SANS patterns of PTB7 solutions in DCB and DCB:DIO appear totally different from those of PC₇₁BM solutions. The SANS curves for PTB7 solutions were modeled using a worm-like chain model with an excluded volume effect under the assumption that PTB7 assumes a semi-rigid chain nature in good solvents. Since the SANS curves for both PTB7 solutions in DCB and DCB:DIO are almost identical within the error range, a single set of model parameters was applied to fit both curves. The fit parameters, including contour length (L), Kuhn length (b_i), and diameter (R), are tabulated in Table 2. The L is about ~ 395 Å, a molecular dimension much larger than that of PC₇₁BM. The molecular diameter of PC₇₁BM is known to be ~ 11 Å.³² It is apparent that the different scattering features of PTB7 and PC₇₁BM solutions are due to their different molecular sizes and shapes. A schematic diagram showing the possible molecular conformation of PTB7 dissolved in the solvents is shown in Fig. 2b. The identical SANS curves for both PTB7 solutions indicate that the PTB7 chains have an identical swollen or dissolved state regardless of the presence of DIO. Therefore, the SANS results clearly demonstrate that the improved PCEs in both i-OSCs and c-OSCs do not originate from their initial precursor structures in solution.

In order to investigate the effect of the DIO additive on the phase morphology, the PTB7:PC₇₁BM films spun-cast from solutions with and without DIO were sectioned using a focused ion beam (FIB), and the exposed cross-sections were imaged by energy-filtered transmission electron microscopy (EF-TEM). Fig. 3 shows the cross-section images of PFN/PTB7:PC₇₁BM and PEDOT:PSS/PTB7:PC₇₁BM with and without DIO, where the yellow and grey areas indicate PC₇₁BM-rich and

Table 2 Parameters obtained from the model fits for PTB7 chains dissolved in DCB and DCB:DIO. Since SANS curves for PTB7/DCB and PTB7/DCB:DIO solutions are almost identical to each other with a negligible difference, the same fit parameters were used to fit the curves

	Contour length, L (Å)	Kuhn length, b_i (Å)	Radius, R (Å)	Polydispersity
PTB7 in DCB & DCB:DIO	395 ± 5	183 ± 3	10.7 ± 0.3	0.089 ± 0.035

PTB7-rich regions, respectively. The films exhibit much reduced domain sizes when DIO is used as a processing additive, consistent with the results reported in the literature.^{9,33} Nevertheless, in terms of the domain size of PC₇₁BM, no clear difference between PFN/PTB7:PC₇₁BM and PEDOT:PSS/PTB7:PC₇₁BM films with or without DIO was identified, implying no significant effect of the substrate on the sizes of PTB7 and PC₇₁BM domains. It is obvious that since the interfacial area between PTB7 and PC₇₁BM increases with decreasing domain size, more efficient charge generation is possible as DIO is added to the casting solution resulting in smaller domains. It should be noted that no clear indication of the PFN layer is observed in the TEM images of PFN/PTB7:PC₇₁BM regardless of the presence of DIO, while flat interfacial boundaries are clearly identified between PTB7:PC₇₁BM and PEDOT:PSS layers in PEDOT:PSS/PTB7:PC₇₁BM films both with and without DIO.

It is well known that no diffusion of PC₇₁BM into the PEDOT:PSS layer occurs in spin-casting or thermal annealing,³⁴ which is indeed not preferable, since it would prevent the hole transport to the anode, giving rise to a reduction in PCE. The absence of the PFN layer in the EF-TEM images of the PFN/PTB7:PC₇₁BM cross-sections is due to the intermixing between PC₇₁BM and PFN, as will be shown in the following section.

To investigate the vertical phase morphologies, neutron reflectivity (NR) measurements were performed on PTB7:PC₇₁BM films deposited onto PFN-coated substrates. Fig. 4a shows the experimental and fitted NR curves for PFN/PTB7:PC₇₁BM films, which were prepared by spin-casting PTB7:PC₇₁BM solutions with and without DIO on top of PFN films. As a reference, experimental and fit NR curves for an ~8 nm thick pristine PFN film are also included in Fig. 4a. Fitting to the experimental NR curves were performed using Parratt formalism,³⁵ from which the obtained neutron scattering length density (SLD) distributions and the composition distributions of PC₇₁BM ($V_{PC_{71}BM}$), calculated from the SLD distributions, are depicted in Fig. 4b and c, respectively. $V_{PC_{71}BM}$ of each layer was calculated using eqn (S1) and (S2), shown in the ESI.† As seen in Fig. 4b, the PFN film consists of two layers with different SLDs, *i.e.*, $\rho_{PFN} = 0.83 \times 10^{-6}$ and $1.14 \times 10^{-6} \text{ \AA}^{-2}$. This could be due to the phase separation of copolymeric PFN, where the higher SLD could be due to the enrichment of poly[[9,9-bis(3'-(*N,N*-dimethylamino)propyl)-2,7-fluorene]] with a short side chain, and the lower SLD to that of poly[2,7-(9,9-dioctylfluorene)] with its long alkyl side chain. The SLDs of

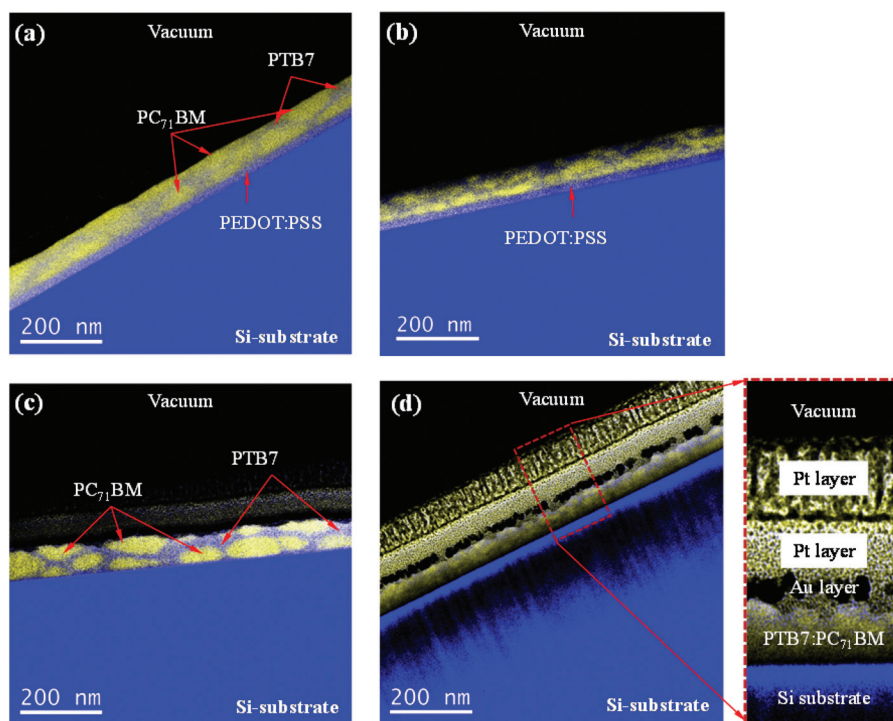


Fig. 3 Cross-section TEM images of PEDOT:PSS/PTB7:PC₇₁BM films (a) without and (b) with 3 wt% DIO; and PFN/PTB7:PC₇₁BM films (c) without and (d) with 3 wt% DIO.

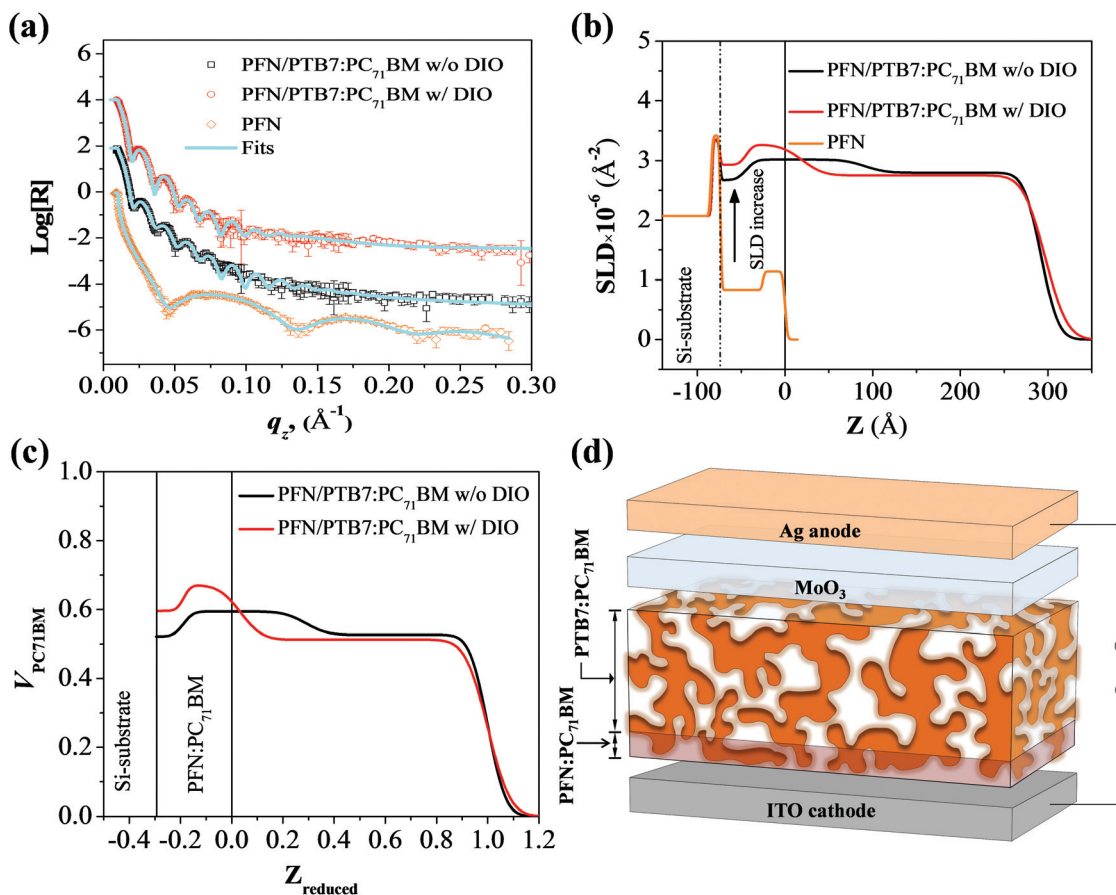


Fig. 4 (a) Experimental and modeled NR curves for PFN/PTB7:PC₇₁BM films with and without DIO. (b) The SLD profiles used to fit the NR curves shown in (a). (c) Volume fraction profiles of PC₇₁BM vs. reduced distance from the substrate, calculated from the SLD profiles shown in (b). (d) Schematic illustration showing how PC₇₁BM diffuses into the PFN layer.

PFN layers increase drastically after spin-casting PTB7:PC₇₁BM. In the film spun-cast without DIO, the SLDs of PFN layers increase from $\rho_{\text{PFN}} = 0.83 \times 10^{-6}$ and $1.14 \times 10^{-6} \text{\AA}^{-2}$ to 2.67×10^{-6} and $3.02 \times 10^{-6} \text{\AA}^{-2}$, respectively. With DIO, the PFN SLDs increase even more to 2.93×10^{-6} and $3.26 \times 10^{-6} \text{\AA}^{-2}$. Since the increased SLDs of PFN after spin-casting are higher than those of PTB7 ($\rho_{\text{PTB7}} = 1.26 \times 10^{-6} \text{\AA}^{-2}$) and PFN ($\rho_{\text{PFN}} = 0.83 \times 10^{-6}$ and $1.14 \times 10^{-6} \text{\AA}^{-2}$), the increases in SLDs can only be attributed to the diffusion of high-SLD PC₇₁BM. The SLD of PC₇₁BM is $\rho_{\text{PC71BM}} = 4.34 \times 10^{-6} \text{\AA}^{-2}$ as shown in Fig. S3 and 4.† The calculated V_{PC71BM} , with the PFN layer underneath, using eqn (S2),† are 0.52 and 0.59 in PFN/PTB7:PC₇₁BM without using DIO, and are 0.60 and 0.67 with DIO. The diffusion of PC₇₁BM into the PFN layer occurs when the residual solvent molecules (DCB or DCB:DIO) that remain in the films act as plasticizers and make PC₇₁BM molecules mobile. Based on the TEM cross-section images (Fig. 3) and NR results (Fig. 4), a schematic illustration of the i-OSC active layer morphology is depicted in Fig. 4d. Here, the diffusion of PC₇₁BM into PFN layers has a very important implication on the device efficiency, since it can alter the process of electron transport. That is, the diffusion of PC₇₁BM into PFN layers and the phase-separated domain formation of PC₇₁BM can

produce much more interfacial contacts between PC₇₁BM and PFN. Also, the increased PC₇₁BM diffusion induced by the added DIO facilitates even more interfacial contacts between PC₇₁BM and PFN, resulting in a more efficient electron transport to the cathode and electron collection.

In order to confirm the aforementioned hypothesis, PTB7:PC₇₁BM solutions in DCB with and without DIO were spun-cast onto bare quartz substrates and dried completely, followed by PFN spin-casting. The measured and fitted NR curves for PTB7:PC₇₁BM/PFN films spun-cast with and without DIO are depicted in Fig. 5a, from which the acquired SLD and V_{PC71BM} distributions are shown in Fig. 5b and c, respectively. As can be seen in Fig. 5b, the SLDs of PFN layers in both PTB7:PC₇₁BM/PFN films remain unchanged compared to that of pristine PFN films. Also, the SLDs of PTB7:PC₇₁BM layers in PTB7:PC₇₁BM/PFN films with and without DIO are identical to those of PTB7:PC₇₁BM-only films (Fig. S3†). The results reveal that the diffusion of PC₇₁BM does not occur in PTB7:PC₇₁BM/PFN films, since no DCB or DCB:DIO remains in the film. The film probably contains residual methanol after spin-casting PFN solution (in methanol), however, methanol is a non-solvent for PC₇₁BM, and hence it cannot act as a plasticizer for PC₇₁BM diffusion.

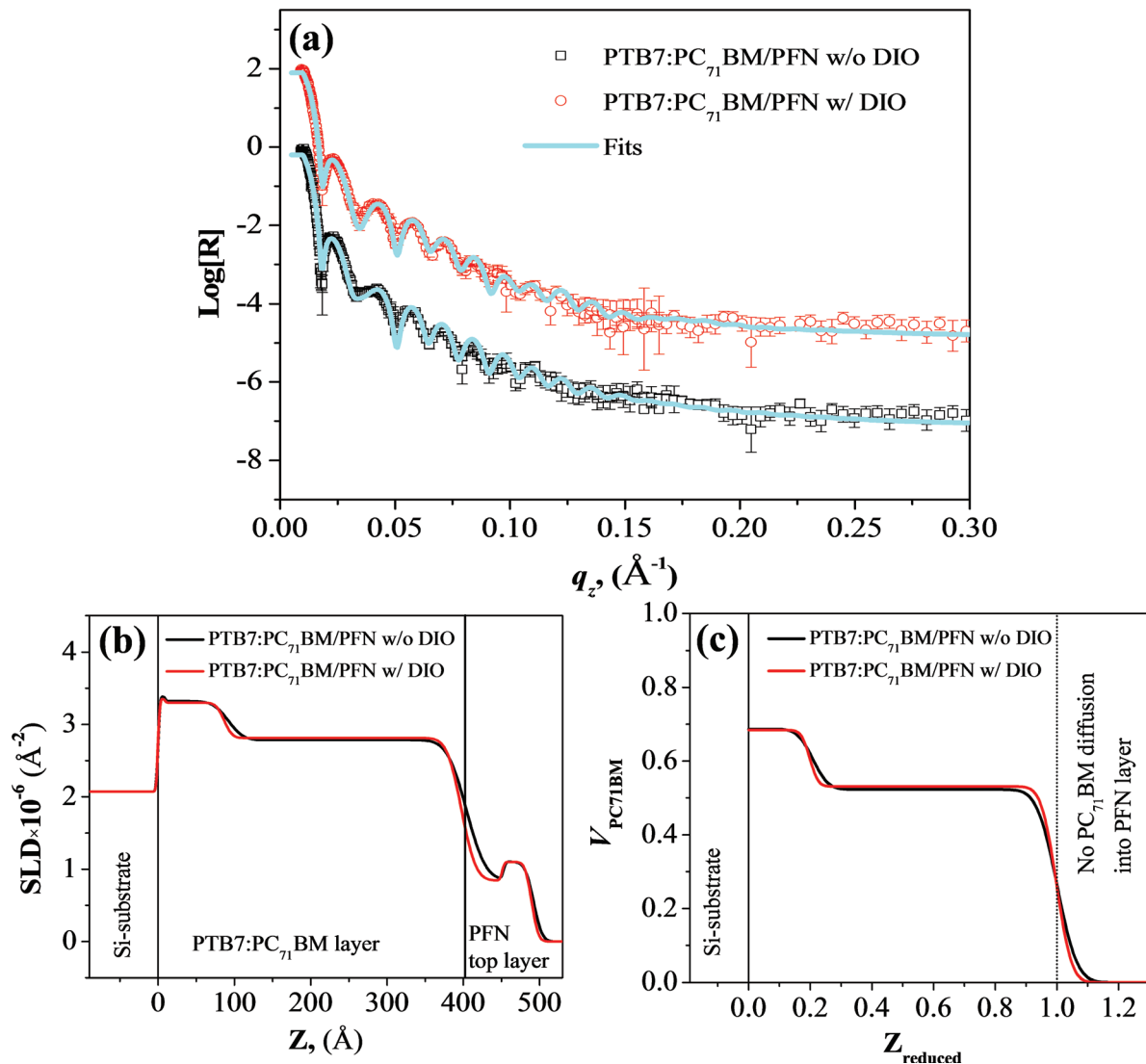


Fig. 5 (a) Experimental and modeled NR curves for PTB7:PC₇₁BM/PFN films with and without DIO. (b) The SLD profiles used to fit the NR curves shown in (a). (c) Volume fraction profiles of PC₇₁BM vs. reduced distance from the substrate, calculated from the SLD profiles shown in (b).

Two-dimensional (2D) grazing-incidence wide-angle X-ray scattering (GIWAXS) was used to obtain insights into the global orientation, molecular packing, and crystallinity of PTB7, as well as the aggregation of PC₇₁BM. A 2D GIWAXS pattern for PFN/PTB7 is first shown in Fig. 6a. Here, q_y is the in-plane scattering vector given by $q_y = 2\pi/\lambda_x[\sin(\psi)\cos(\alpha_f)]$, where λ_x , ψ , and α_f are the wavelength, in-plane exit angle, and out-of-plane exit angle, respectively. In the 2D GIWAXS pattern, the in-plane reflection arcs discerned at $q_y = 0.283 \pm 0.008 \text{ \AA}^{-1}$ (d -spacing = 22.2 \AA) are due to the (100) planes of PTB7 crystals. A broad out-of-plane reflection arc was also observed at $q_z = 1.56 \pm 0.05 \text{ \AA}^{-1}$ (d -spacing = 4.1 \AA), which is indexed by (010) reflection. The broad in-plane (100) and out-of-plane (010) reflection indicates that the planes of PTB7 aromatic backbones are roughly aligned parallel to the surface plane of the substrate with the alkyl side chains directed toward the in-plane direction. This orientation is the so-called ‘face-on’

orientation of PTB7 crystals. While the face-on orientation of PTB7 crystals is desired for high PCE, it is not the case in the blend films as addressed in the 2D GIWAXS patterns depicted in Fig. 6b and c. In the 2D patterns of the blend films, the observed (100) reflection rings imply random orientation of PTB7 crystals. The broad reflection halos centered at $q \approx 1.37 \text{ \AA}^{-1}$ (d -spacing = 4.7 \AA), on the other hand, are attributed to the short range ordering of randomly oriented PC₇₁BM crystals, *i.e.*, (311) reflection. The random orientation of PTB7 and PC₇₁BM crystals could possibly implicate that the growth process of oriented PTB7 and PC₇₁BM crystals is impeded by each other during the film formation process. One of the most notable features (Fig. 6d) is that the in-plane GIWAXS slices for PFN/PTB7:PC₇₁BM films cast with and without DIO almost overlap with each other, indicating the same degree of crystallinity. Our results are in agreement with previous reports.^{33,36} More importantly, the result indicates that the improved PCEs

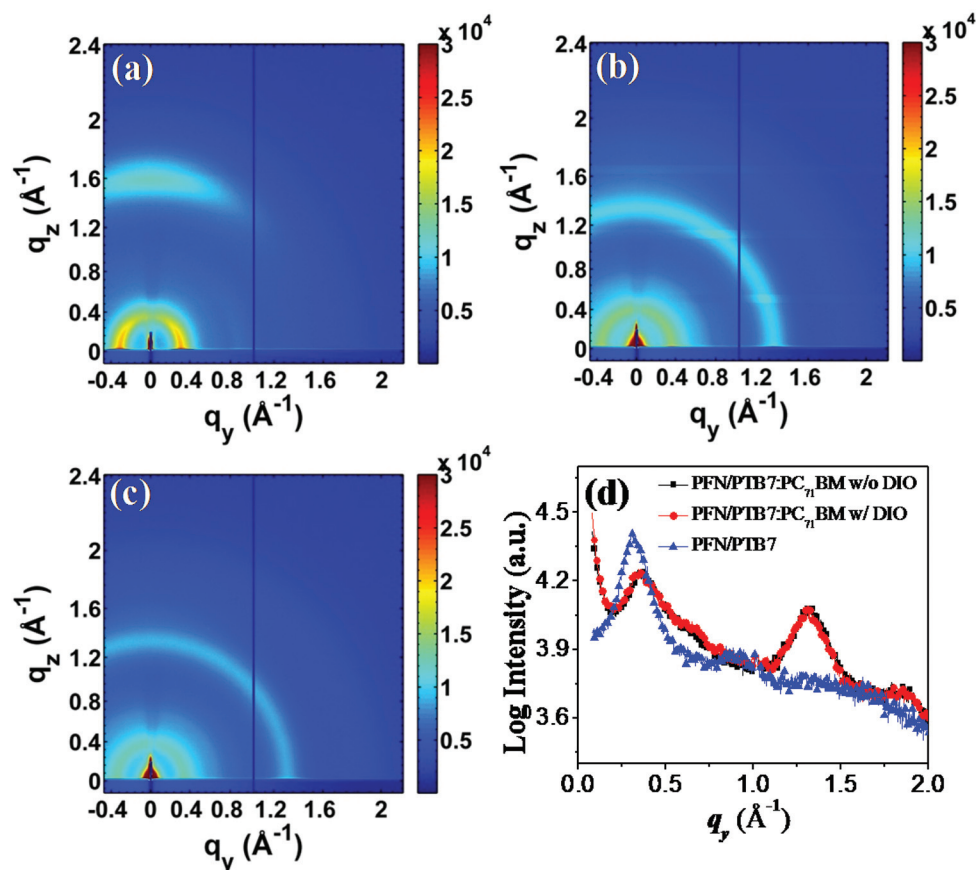


Fig. 6 2D GIWAXS patterns of (a) PFN/PTB7, (b) PFN/PTB7:PC₇₁BM without DIO, and (c) PFN/PTB7:PC₇₁BM with DIO films. (d) In-plane GIWAXS profiles extracted from the respective 2D GIWAXS patterns.

resulted from the DIO additive in neither the i-OSCs nor the c-OSCs based on PTB7:PC₇₁BM active layers are related to crystallinity and orientation morphology.

In summary, the nanoscale structural aspects of high PCE of PTB7:PC₇₁BM i-OSCs using PFN as the ITO modifier were investigated. SANS results of PTB7 and PC₇₁BM solutions indicate that both PTB7 and PC₇₁BM remain in completely dissolved states in both pristine DCB and DCB:DIO; no effect of DIO on the solution morphologies was identified. In the spun-cast films, however, DIO was found to play a vital role in the morphological evolution occurring during the film formation process after spin-casting. In both i-OSCs and c-OSCs, the DIO added to the casting solutions induces the formation of much smaller PTB7 and PC₇₁BM domains, which was revealed by cross-section TEM. The formation of smaller PC₇₁BM domains forms the basis for more efficient exciton transport to the PTB7/PC₇₁BM interface and more effective charge separation at the interface. In i-OSCs, PC₇₁BM was found to diffuse into the PFN layer as the casting solutions are spun-cast on top of the PFN layer, where more PC₇₁BM diffusion occurs when DIO is added to the casting solutions. The increased PC₇₁BM diffusion into the PFN layer increases the interfacial contact between PC₇₁BM and PFN, and hence improves electron transport and collection at the cathode, increasing the PCE.

Acknowledgements

This research was conducted at the Center for Nanophase Materials Sciences (CNMS) and Spallation Neutron Source (SNS), which are sponsored at Oak Ridge National Laboratory by the Scientific User Facilities Division, U.S. Department of Energy. Work by Wei Chen was supported by the U.S. Department of Energy, Office of Science, Basic Energy Sciences, Materials Sciences and Engineering Division. This research used resources of the Advanced Photon Source, a U.S. Department of Energy (DOE) Office of Science User Facility operated for the DOE Office of Science by Argonne National Laboratory under Contract No. DE-AC02-06CH11357.

References

- 1 M. Kaltenbrunner, M. S. White, E. D. Głowacki, T. Sekitani, T. Someya, N. S. Sariciftci and S. Bauer, *Nat. Commun.*, 2012, **3**, 770.
- 2 Z. Liu, J. Li and F. Yan, *Adv. Mater.*, 2013, **25**, 4296–4301.
- 3 S. I. Na, S. S. Kim, J. Jo and D. Y. Kim, *Adv. Mater.*, 2008, **20**, 4061–4067.

- 4 B. Zhao, Z. He, X. Cheng, D. Qin, M. Yun, M. Wang, X. Huang, J. Wu, H. Wu and Y. Cao, *J. Mater. Chem. C*, 2014, **2**, 5077–5082.
- 5 G. Li, V. Shrotriya, J. Huang, Y. Yao, T. Moriarty, K. Emery and Y. Yang, *Nat. Mater.*, 2005, **4**, 864–868.
- 6 W. Ma, C. Yang, X. Gong, K. Lee and A. J. Heeger, *Adv. Funct. Mater.*, 2005, **15**, 1617–1622.
- 7 T. A. Bull, L. S. Pingree, S. A. Jenekhe, D. S. Ginger and C. K. Luscombe, *ACS Nano*, 2009, **3**, 627–636.
- 8 J. D. Zimmerman, X. Xiao, C. K. Renshaw, S. Wang, V. V. Diev, M. E. Thompson and S. R. Forrest, *Nano Lett.*, 2012, **12**, 4366–4371.
- 9 Y. Liang, Z. Xu, J. Xia, S. T. Tsai, Y. Wu, G. Li, C. Ray and L. Yu, *Adv. Mater.*, 2010, **22**, E135–E138.
- 10 F. Etzold, I. A. Howard, N. Forler, A. Melnyk, D. Andrienko, M. R. Hansen and F. Laquai, *Energy Environ. Sci.*, 2015, **8**, 1511–1522.
- 11 S. V. Kesava, Z. Fei, A. D. Rimshaw, C. Wang, A. Hexemer, J. B. Asbury, M. Heeney and E. D. Gomez, *Adv. Energy Mater.*, 2014, **4**, 1400116.
- 12 F. Zhang, K. G. Jespersen, C. Bjoerstroem, M. Svensson, M. R. Andersson, V. Sundström, K. Magnusson, E. Moons, A. Yartsev and O. Inganäs, *Adv. Funct. Mater.*, 2006, **16**, 667–674.
- 13 L. Ye, S. Zhang, W. Ma, B. Fan, X. Guo, Y. Huang, H. Ade and J. Hou, *Adv. Mater.*, 2012, **24**, 6335–6341.
- 14 Y. Liu, J. Zhao, Z. Li, C. Mu, W. Ma, H. Hu, K. Jiang, H. Lin, H. Ade and H. Yan, *Nat. Commun.*, 2014, **5**.
- 15 A. T. Yiu, P. M. Beaujuge, O. P. Lee, C. H. Woo, M. F. Toney and J. M. Fréchet, *J. Am. Chem. Soc.*, 2012, **134**, 2180–2185.
- 16 H.-Y. Chen, J. Hou, S. Zhang, Y. Liang, G. Yang, Y. Yang, L. Yu, Y. Wu and G. Li, *Nat. Photonics*, 2009, **3**, 649–653.
- 17 K.-H. Tu, S.-S. Li, W.-C. Li, D.-Y. Wang, J.-R. Yang and C.-W. Chen, *Energy Environ. Sci.*, 2011, **4**, 3521–3526.
- 18 M. A. Green, K. Emery, Y. Hishikawa, W. Warta and E. D. Dunlop, *Prog. Photovoltaics: Res. Appl.*, 2015, **23**, 1–9.
- 19 Z. Xu, L. M. Chen, G. Yang, C. H. Huang, J. Hou, Y. Wu, G. Li, C. S. Hsu and Y. Yang, *Adv. Funct. Mater.*, 2009, **19**, 1227–1234.
- 20 C.-H. Hsieh, Y.-J. Cheng, P.-J. Li, C.-H. Chen, M. Dubosc, R.-M. Liang and C.-S. Hsu, *J. Am. Chem. Soc.*, 2010, **132**, 4887–4893.
- 21 M. T. Dang, L. Hirsch and G. Wantz, *Adv. Mater.*, 2011, **23**, 3597–3602.
- 22 S. K. Hau, H.-L. Yip, N. S. Baek, J. Zou, K. O'Malley and A. K.-Y. Jen, *Appl. Phys. Lett.*, 2008, **92**, 253301.
- 23 C. Waldauf, M. Morana, P. Denk, P. Schilinsky, K. Coakley, S. Choulis and C. Brabec, *Appl. Phys. Lett.*, 2006, **89**, 233517.
- 24 S. K. Hau, H.-L. Yip, O. Acton, N. S. Baek, H. Ma and A. K.-Y. Jen, *J. Mater. Chem.*, 2008, **18**, 5113–5119.
- 25 C. Tao, S. Ruan, X. Zhang, G. Xie, L. Shen, X. Kong, W. Dong, C. Liu and W. Chen, *Appl. Phys. Lett.*, 2008, **93**, 193307.
- 26 Z. He, C. Zhong, S. Su, M. Xu, H. Wu and Y. Cao, *Nat. Photonics*, 2012, **6**, 591–595.
- 27 Z. He, B. Xiao, F. Liu, H. Wu, Y. Yang, S. Xiao, C. Wang, T. P. Russell and Y. Cao, *Nat. Photonics*, 2015, **9**, 174–179.
- 28 B. Yang, Y. Yuan and J. Huang, *J. Phys. Chem. C*, 2014, **118**, 5196–5202.
- 29 O. E. Semonin, J. M. Luther, S. Choi, H.-Y. Chen, J. Gao, A. J. Nozik and M. C. Beard, *Science*, 2011, **334**, 1530–1533.
- 30 J. K. Keum, K. Xiao, I. N. Ivanov, K. Hong, J. F. Browning, G. S. Smith, M. Shao, K. C. Littrell, A. J. Rondinone, E. A. Payzant, J. Chen and D. K. Hensley, *CrystEngComm*, 2013, **15**, 1114–1124.
- 31 M. Shao, J. K. Keum, R. Kumar, J. Chen, J. F. Browning, S. Das, W. Chen, J. Hou, C. Do, K. C. Littrell, A. Rondinone, D. B. Geohegan, B. G. Sumpter and K. Xiao, *Adv. Funct. Mater.*, 2014, **24**, 6647–6657.
- 32 S. J. Lou, J. M. Szarko, T. Xu, L. Yu, T. J. Marks and L. X. Chen, *J. Am. Chem. Soc.*, 2011, **133**, 20661–20663.
- 33 M. R. Hammond, R. J. Kline, A. A. Herzing, L. J. Richter, D. S. Germack, H.-W. Ro, C. L. Soles, D. A. Fischer, T. Xu, L. Yu, M. F. Toney and D. M. DeLongchamp, *ACS Nano*, 2011, **5**, 8248–8257.
- 34 H. Lu, B. Akgun and T. P. Russell, *Adv. Energy Mater.*, 2011, **1**, 870–878.
- 35 L. G. Parratt, *Phys. Rev.*, 1954, **95**, 359.
- 36 B. A. Collins, Z. Li, J. R. Tumbleston, E. Gann, C. R. McNeill and H. Ade, *Adv. Energy Mater.*, 2013, **3**, 65–74.